Check for updates

Optical coherence microangiography of the mouse kidney for diagnosis of circulatory disorders

ARKADY S. ABDURASHITOV,[1,7] (iD) EKATERINA S. PRIKHOZHDENKO,[2] (iD) OKSANA A. MAYOROVA,[2] (iD) VALENTINA O. PLASTUN,[2] OLGA I. GUSLIAKOVA,[2] NATALIA A. SHUSHUNOVA,[2] OLEG A. KULIKOV,[3] VALERY V. TUCHIN,[2,4,5] (iD) GLEB B. SUKHORUKOV,[1,6] AND OLGA A. SINDEEVA[1,2,8] (iD)

[1]*Skolkovo Institute of Science and Technology, Skolkovo Innovation Center, 3 Nobel str., Moscow 143005, Russia*
[2]*Science Medical Center, Saratov State University, 83 Astrakhanskaya str., Saratov 410012, Russia*
[3]*Ogarev Mordovia State University, 68 Bolshevistskaya str., Saransk 430005, Russia*
[4]*Interdisciplinary Laboratory of Biophotonics, National Research Tomsk State University, 36 Lenina Avenue, Tomsk 634050, Russia*
[5]*Laboratory of Laser Diagnostics of Technical and Living Systems, Institute of Precision Mechanics and Control of the Russian Academy of Science, 24 Rabochaya Str., Saratov 410028, Russia*
[6]*School of Engineering and Materials Science, Queen Mary University of London, Mile End, Eng, 215, London E1 4NS, United Kingdom*
[7]*a.abdurashitov@skoltech.ru*
[8]*o.sindeeva@skoltech.ru*

Abstract: Optical coherence tomography (OCT) has become widespread in clinical applications in which precise three-dimensional functional imaging of living organs is required. Nevertheless, the kidney is inaccessible for the high resolution OCT imaging due to a high light attenuation coefficient of skin and soft tissues that significantly limits the penetration depth of the probing laser beam. Here, we introduce a surgical protocol and fixation scheme that enables functional visualization of kidney's peritubular capillaries via OCT microangiography. The model of reversible/irreversible glomerulus embolization using drug microcarriers confirms the ability of OCT to detect circulatory disorders. This approach can be used for choosing optimal carriers, their dosages and diagnosis of other blood flow pathologies.

1. Introduction

Optical coherence microangiography (OCMA) is a label-free tool for *in vivo* monitoring of vascular structures within different organs [1]. Analysis of time-varying components in the optical coherence tomography (OCT) signal is used to segment blood vessels from surrounding tissues [2–4]. High sensitivity to small changes in blood flow and outstanding spatial resolution of OCMA allows the detection of microvessels (with size <20 μm) and their responses to different stimuli. However, due to large scattering and light absorption such a high spatial resolution could only be maintained within the first few hundreds micrometers deep inside the tissue. This value could be improved by utilizing near/mid infrared light sources or by applying an optical clearing solution to temporarily reduce the light scattering coefficient [5,6]. Nevertheless, the vital internal organs still cannot be directly visualized by conventional OCT setups, since they usually lie at a depth of several millimeters, even in small animals. Specialized OCT systems like endoscopic [7] or needle based [8] could provide a limited *in vivo* capability in case of deep organs imaging but with lower spatial resolution and scanning speed. In order to be able to

perform high quality imaging of deeply lying organs, an attenuation free path should be provided for the probing laser beam. One way to do this is to make a small surgical incision to expose the organs being examined. It is important to separate the major movements of the sample due to breathing, heartbeat, or random muscle contractions from erythrocyte motions within the blood vessels that generate a useful OCMA signal. This can be done by using expensive OCT setups with a high data acquisition rate or by developing the correct fixation scheme for the organ under study. This method of fixation should ensure high temporal stability of the organ, as well as normal blood flow circulation without any clamping-induced restrictions.

The kidney is one of the most important internal organs, which is located relatively deep inside the body and performs several vital tasks: filtering blood, maintaining acid-base balance, removing toxins. Kidney related diseases often become chronic and, in the absence of timely diagnostics and effective treatment, can lead to end-stage renal disease [9]. The early stages of many kidney diseases are hidden and asymptomatic and are often associated with blood flow pathological changes [10–12]. This fact makes it extremely important to perform high-precision functional imaging of renal vessels to search for early markers of specific diseases or monitor the effect of newly developed treatment regimens.

There are several articles describing structural OCT imaging of kidney either *in situ* [13,14] or *in vivo* through surgical incision without clamp to isolate movement [15]. Functional imaging of renal vessels is usually performed using OCT in Doppler mode [16], which is highly sensitive to phase noise and requires sophisticated phase-unwrapping algorithms to perform proper velocity estimation in post-processing.

In this article, we have described a protocol for label-free high-precision volumetric functional imaging of kidney superficial vessels *in vivo*, using optical coherency microangiography and proper fixation scheme, which provides required motion isolation and does not interfere with normal blood circulation in the kidney. To verify the applicability of the proposed method, blood flow studies were carried out using the model of reversible/irreversible embolization, in which renal artery injection of microcontainers of different concentration was used to induce glomerular blood flow failure.

Studying the effect of microcontainers on the blood supply to vital organs is in itself also an important task of nanomedicine [17], especially in the context of their intra-arterial targeting. One of the options of such microcontainers can be biocompatible polyelectrolyte microcapsules. They are highly stable [18], can carry various drugs [19,20] and labels [21–23], and are able to provide a prolonged release of the cargo [24]. Microcapsules have a sufficiently large size to mechanically linger in the capillaries. Unlike microparticles, they do not contain a rigid core that allow them to change shape while passing through small capillaries [25]. As we showed previously, same-sized capsules are able to accumulate in mesentery [26] and muscle [27] capillaries under the magnetic field traction without irreversible blood flow blocking. The combination of these features allowed us to select microcapsules based on biocompatible polyelectrolytes as microcontainers to model reversible/irreversible embolization of blood flow in renal glomeruli.

2.   Material and methods

2.1.   Materials

Sodium carbonate (anhydrous), calcium chloride (dihydrate), ethylenediaminetetraacetic acid disodium salt (EDTA, dihydrate), bovine serum albumin (BSA, lyophilized powder), rhodamine B isothiocyanate (RITC), poly-L-arginine hydrochloride (pArg, MW>70 000), dextran sulfate sodium salt (DsS, MW>70 000), phosphate-buffered saline (PBS, 0.01 M) were purchased from Sigma-Aldrich (Germany). Hydrochloric acid was obtained from Reakhim (Russia). Dimethyl sulfoxide (DMSO) was purchased from Merck (Germany). Cyanine 7 NHS ester (Cy7) was obtained from Lumiprobe (Russia). Sucrose was purchased from Ecokhimanalit (Russia). Formalin solution was obtained from Vecton (Russia). All reagents were used as received without
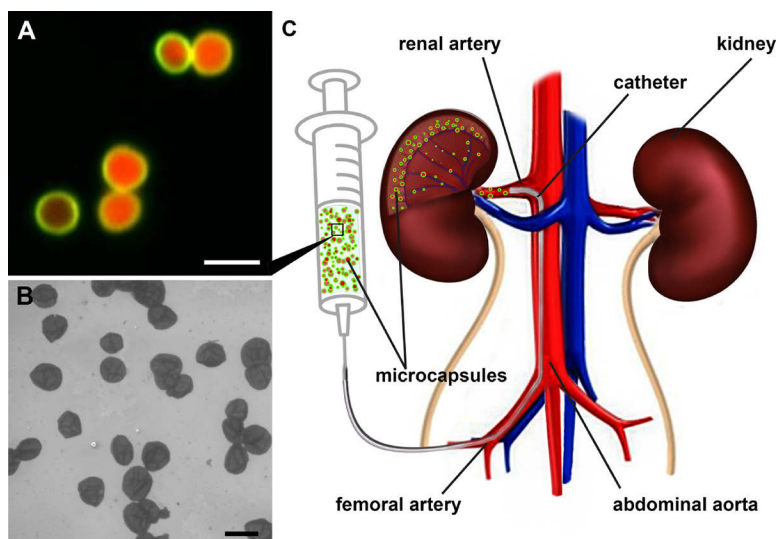
Fig. 1. CLSM images of polyelectrolyte microcapsules in aqueous solution. Green — shell labeled with BSA-RITC. Red — encapsulated cargo (BSA conjugated with Cy7) (A). SEM images of collapsed polyelectrolyte microcapsules after drying demonstrates the absence of a solid core (B). General scheme for microcapsule targeting on mouse kidney via the renal artery (C). Scale bar, 5 μm.

further purification. Millipore Milli Q water (18.2 MΩ·m^{-1}) was used as an aqueous medium during all sets of experiments.

2.2. Microcapsule synthesis and characterization

Fluorescent biocompatible microcapsules were prepared according to our previous work [28]. The inner space of the hollow microcapsules contains the Cy7-BSA conjugate as cargo. The composition of the shell was as follows: [pArg/DsS/pArg/RITC-BSA/pArg/DsS] (Fig. 1(A)).

Confocal Laser Scanning Microscopy (CLSM) was performed using a Leica TCS SP8 X (Leica Microsystems, Germany) to study the fluorescent properties of as-prepared microcapsules. This setup is equipped with a white light pulsed laser with the capability to choose excitation wavelength from 470–670 nm range with 1 nm precision. The laser was focused through 20×/0.70 N.A. objective (Leica Microsystems, Germany). RITC was excited by the 554 nm laser with the 570–650 nm detection range (green color); Cy7 was excited by the 670 nm laser with the 700–795 nm detection range (red color). Microcapsules size distribution was evaluated using 300 CLSM images and was 3.96±0.63 μm (see Fig. S1 in Supplement 1).

Scanning Electron Microscopy (SEM) measurements were executed with a VEGA III (TESCAN, Czech Republic) microscope at an operating voltage of 30 kV. SEM images are typical of microcapsules (Fig. 1(B)). It confirms the absence of a rigid core.

2.3. Renal artery injection of microcapsules

The laboratory animals were treated according to the rules of Saratov State Medical University (Ethics Committee protocol no. 7 dated 02.02.2021), the Geneva Convention of 1985 (International Guiding Principles for Biomedical Research Involving Animals). All experimental procedures were performed on white Balb mice 6–8 weeks old (20–25 g weight) using general anesthesia (Zoletil mixture (40 mg per kg, 50 μL, Virbac SA, Carros, France) and 2% Rometar (10 μL and 10 mg per kg, Spofa, Czech Republic) via intraperitoneal injection). The number

of mice in each group was 3. At the end of the experiment, the animals were euthanized by an overdose of anesthesia.

Microcapsules suspension was addressed to the kidney directly through the renal artery using polyethylene catheter (PE-10, Scientific Commodities INC., Lake Havasu City, Arizona) with thin polyurethane intravascular tubing on the end (40 mm, PU tubing, 32ga/.8Fr, 0.005×0.010 in, Instech). A thin part of the saline-filled catheter was implanted through the right femoral artery into the abdominal aorta and then we carefully inserted the end of the catheter (1.5–2 mm) into the left renal artery. The localization of the catheter and its navigation within the arterial bed were monitored through a small incision (8–10 mm) made parallel to the spine (2–3 mm from it) above the kidney. 10 μL of the capsule suspension were injected into the renal artery in the selected dosage (taking into account the catheter "dead volume"). The renal artery walls were tightly clamped to the catheter walls using tweezers to prevent capsules entering the aorta during injection. A minute later, the tweezers were opened and the catheter was carefully removed from the vascular bed. More details of the capsule injection procedure can be found in our previous work [28]. Dosages of microcapsules were adjusted to 10×10^6 and 20×10^6 per injection due to their larger size. General scheme of microcapsules injection is in Fig. 1(C).

Note, that we only compromised the integrity of the femoral artery for catheter insertion. Further movement of the catheter was carried out within the arterial bed without damaging the integrity of the aorta or renal artery. This eliminates the possibility of bleeding and damage to the blood supply to the kidney due to the operation itself. The renal artery diameter is slightly larger than the catheter diameter, due to which the blood can enter the kidney in a small amount when the catheter is located in it. A similar procedure is performed in clinical practice for the local targeting of contrast agents and drugs [29], as well as for the intravascular implants installation [30].

2.4. Optical coherence tomography

Optical coherence tomography (OCT) of the kidney surface was implemented *in vivo* to track changes in the organ blood flow as a result of microcapsule injection. OCT measurements were performed on the same animals under general anesthesia before, 15 min, 1 hour, and 24 hours after renal artery injection of microcapsules. To monitor blood flow circulation in peritubular vessels of kidney, commercially available OCT system GANYMEDE with following specs was used: central wavelength of light source — 930 nm, optical bandwidth — 150 nm, A-scan rate — 30 kHz, laser spot size — 12 μm, 4 consequent B scan were obtained in one spatial location of the kidney to perform pixel-wise speckle variance analysis. Peritubular vessels network was reconstructed in 3D from 1×1×0.07 mm of the kidney's top layer. To enhance the SNR (signal to noise ratio) a histogram equalization routine was implemented. A few ROI were manually placed on the image such that there are no blood vessels inside them. A mean value of signal intensity in these ROIs was used as the lower limit for linear histogram equalization. After that to reduce the "sand"-like noise a median filter with a kernel size of 3×3 was applied to the image. To further enhance vessel contrast and perform its segmentation a Frangi filter (scikit-image package v.0.17.1 of Python base version 3.6) with sigmas ranging from 1 to 3 was used (see Fig. S2 in Supplement 1).

2.5. Histological study

Kidneys were subjected to histological examination 24 h and 120 h (5 days) after left renal artery injection of microcapsules (10×10^6 and 20×10^6). Tissue samples were fixed in neutral formalin. Then the samples were desiccated by dehydrated isopropyl alcohol and embedded in paraffin. The 5-μm thick slides were stained with hematoxylin and eosin. Morphologic analysis of histological samples was performed using an Olympus digital image analysis system.
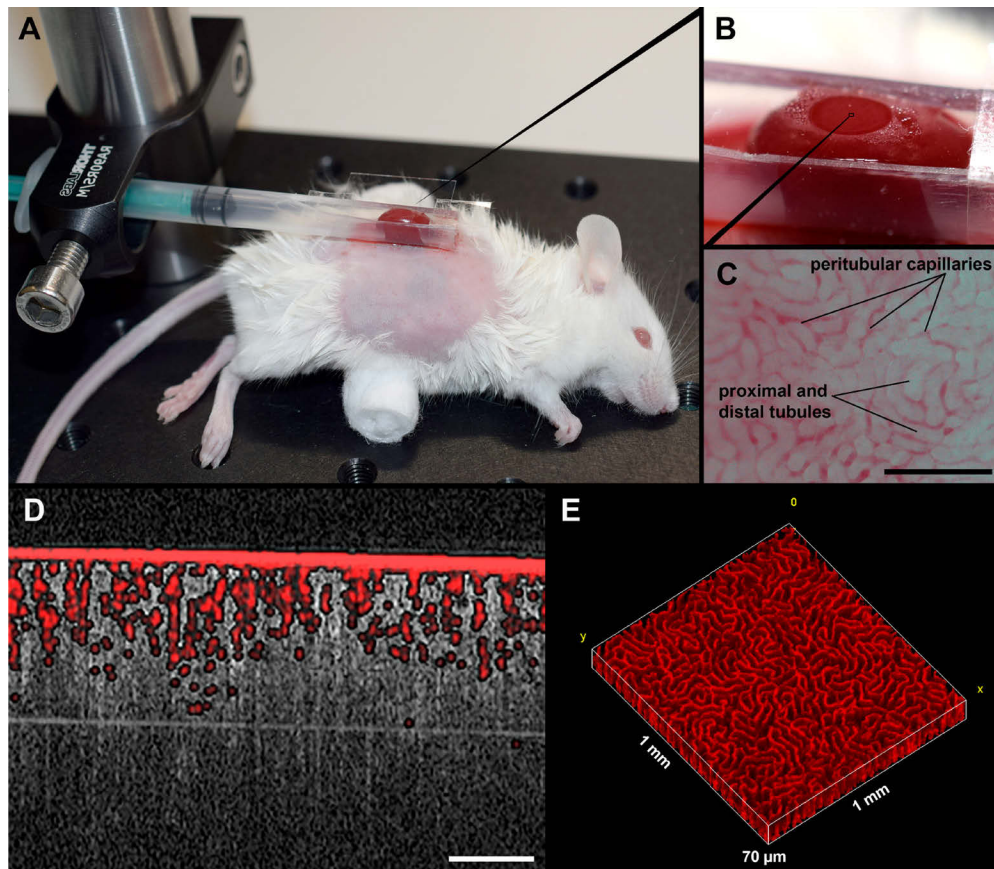
Fig. 2. Mouse fixation scheme to isolate the kidney from breathing movements. The fixation system allows clear visualization of renal peritubular capillaries by optical methods, while maintaining renal blood flow (A). Enlarged photo of the examined area of the kidney (B). Bright-field microscopy image of the mouse kidney surface with peritubular capillaries surrounding the cortical parts of the proximal and distal tubules (C). 2D image (D) and 3D reconstruction (E) of renal peritubular vessels obtained by OCT. Scale bar on C and D, 200 µm.

2.6. *Kidney cryosection study*

Left kidneys after renal artery injection of microcapsules were exposed in a 10% formalin solution for 24 hours. Then the samples were immersed in PBS buffer (7 days), 10, 20, and 30% sucrose solutions in PBS buffer (2 hours each) for cryoprotection and preservation of tissues. Cryosections of kidney tissue with 70 µm thickness were prepared with the Leica CM1950 cryostat (Germany). 3D scans of cryosections were performed via CLSM using Leica TCS SP8 X microscope with laser sources focused through 20×/0.70 N.A. objective. The tissue autofluorescence was excited by 405 nm diode laser with 415–500 nm detection range (blue color); RITC was excited by 554 nm laser with 570–650 nm detection range (green color). Maximum intensity projections were used to generate 2D representations of 3D scans.

3. Results and discussion

3.1. Optical coherence microangiography of mouse kidney superficial vessels

To ensure high spatial and temporal stability of the kidney, it was fixed with a custom clamp made out of 1 mL syringe (Fig. 2(A, B)). We used a cover-slip glass which gently flatten the surface of the kidney to ensure no optical focus related signal losses due to high N.A. scan lens. White light optical image of the kidney was obtained using 10×/0.25 N.A. objective lens prior OCT studying to be sure in free and unrestricted erythrocytes motion within the vessel beds (see Visualization 1). In Fig. 2(C) the peritubular capillaries (dark red) and proximal/distal tubules (white) are clearly distinguished. Peritubular capillaries of the kidney are thin blood vessels supplied by the efferent arteriole of renal glomerulus. These capillaries surround the cortical parts of the proximal and distal tubules in the renal cortex allowing reabsorption and secretion between blood and the inner lumen of the nephron [31].

Proposed fixation scheme allows us to obtain a volumetric dataset that is completely free of motion-related artifacts and requires almost no post-processing procedures to correct them. For high precision measurements of small capillaries (<10 μm) described clamping approach could be empowered with a modern software motion estimation, correction and vessels enchantments algorithms [32–34] to further increase the SNR of the imaging setup.

From the obtained dataset, functional 2D (Fig. 2(D)) or 3D (Fig. 2(E)) microangiographic maps can be easily reconstructed using pixel-wise variance calculation. A global fixed intensity threshold was applied through all obtained microangiographic maps and volumetric vessel density parameters (the ratio between pixels corresponding to the vessels and surrounding tissues) were calculated.

3.2. Volumetric blood vessel density changes of the target kidney after microcapsule injection via renal artery

Microcapsules injection into the left renal artery was accompanied by a significant change in peritubular capillar's density for both doses (10×10^6 and 20×10^6 capsules per mouse, Fig. 3(A, B). However, the decrease in density 15 min after procedure was more significant in the case of the 20×10^6 capsules injection in comparison with the 10×10^6 capsules (density decreased by 73.3% and 46.3% respectively, relative to the basal values). Nevertheless 1 hour later, the positive trend towards kidney's blood supply restoration was registered after injection of lesser dose (the density was reduced only by 18.5% in comparison with the basal values). After 24 hours, the blood supply was completely restored in all mice in the group. In the group with a higher dosage (20×10^6 capsules per mouse), the density remained low and was below the basal value by 76.0 and 73.9% after 1 and 24 hours, respectively.

The morphological state of the kidneys also varied greatly between the high and low dosage in the groups of experimental animals (see Fig. S3 in Supplement 1). The target kidney in mice with a lower dosage (10×10^6 capsules per mouse) had a normal morphological structure both 1 and 5 days after the injection (see Fig. S3 B, D in Supplement 1). The higher dose (20×10^6 capsules per mouse) also did not cause morphological changes in the renal tissue at an early stage (1 day after injection, (see Fig. S3 C in Supplement 1 , despite a strong drop in the density of peritubular vessels recorded with OCT (Fig. 3(A) and (B)). However, after 5 days, we observed pronounced ischemic changes in tissue of target kidney in all animals in this group (see Fig. S3 E in Supplement 1). The differences became even more noticeable after 30 days. Thus, in mice with a low dosage, the targeted and contralateral kidneys had a normal shape, color, and the same size (Fig. 3(C)). In mice with a higher dosage, the strong fibrotic changes of target kidney as a result of ischemia, and contralateral kidney hypertrophy were observed.

Hypertrophy and hyperplasia of the renal tissue is a typical response of the organism to damage to 50% of functioning nephrons [35]. Total or partial ischemia (noted 24 hours after manipulation)
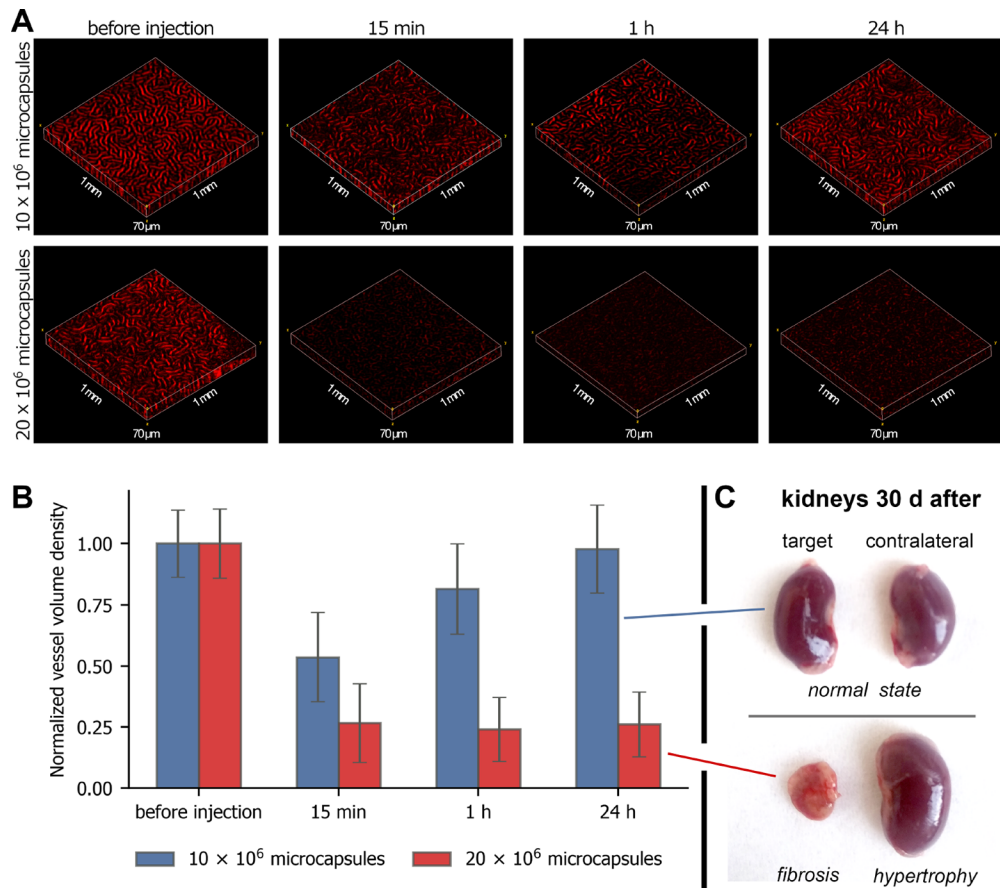
Fig. 3. Dose-dependent changes in the microangiography maps (A, obtained by OCT) and the calculated peritubular capillary density values (B) of the target kidney before and after microcapsules injection via renal artery. Photo of the target (left) and opposite (right) kidneys 30 days after the left renal artery injection of microcapsules in different doses (C). Normal morphological state of the target and the opposite (contralateral) kidney 30 days after the injection of 10×10^6 microcapsules (top). Strong fibrotic changes of target kidney as a result of ischemia, and contralateral kidney hypertrophy as a result of the compensatory reaction after the introduction of microcapsules at a higher dose — 20×10^6 (below).

reduces renal function by half compared to the initial. Hypertrophy and hyperplasia of the contralateral kidney make it possible to compensate the functions of the lost nephrons to a certain degree [36]. However, in some cases, chronic glomerular hypertension and hyperfiltration that develops in the first hours and days after the loss of functions of a large number of nephrons lead to subsequent damage to the preserved nephrons [37]. In this regard, maintaining a normal blood supply to the target kidney is of paramount importance when choosing the microcontainers dosage.

3.3. Effect of accumulation, localization, and migration of microcapsules in the renal cortex affecting its blood supply

In our previous work, we showed that intra-arterial injection of microcapsules leads to their accumulation in the renal cortex, namely, in the glomerular capillaries [28]. We carried out a similar analysis of cortex cryosections in this work in order to explain the mechanisms of

reversible and irreversible changes in superficial peritubular capillaries blood flow associated with the microcapsules accumulation and localization.

The renal cortex images (Fig. 4(A)) clearly show that most of the microcapsules accumulate in the glomeruli (starting from a depth of 400–500 μm from the renal surface to the medulla) even 1 hour after injection. In the area of OCT measurements (0–70 μm from the surface), mainly single capsules in a small amount are detected.
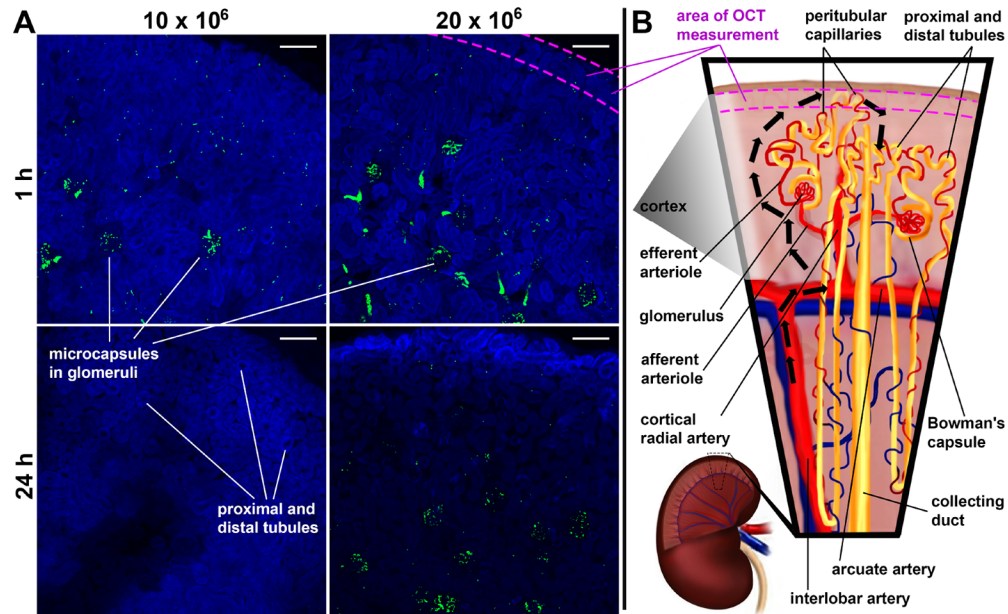

Fig. 4. Cryosections of target kidney cortex 1 and 24 h after microcapsules injection via renal artery in different doses (10×10^6 and 20×10^6 microcapsules). RITC-labeled microcapsule shell (green), tissue autofluorescence (blue). Cryosection thickness, 70 μm; scale bar, 100 μm (A). General scheme of mouse's renal cortex and nephron blood supply (B). Area of OCT measurement marked on cryosection images and scheme using pink dotted line.

This capsules localization can be explained by the peculiarity of the renal blood supply [31]. After injection, all microcapsules enter the renal hilus via the renal artery with blood flow. The renal artery branches form several segmental arteries which immediately branch again into several interlobar arteries (Fig. 4(B)). Of these, the capsules flow into arcuate arteries which pass along the boundary between cortex and medulla. From the arcuate arteries, capsules move out at right angles into the cortex through the cortical radial arteries. These arteries give rise to afferent arterioles which supply the glomerular capillaries (site of filtration of the blood). Here, the capsules get stuck in complexly branched glomerular capillaries. At the same time, they partially or completely block the further movement of blood in efferent arteriole (into a second capillary network).

In normal cases, the efferent arterioles supply the dense network of peritubular capillaries which surround all the cortical tubular elements (proximal and distal tubules). However, blood stops flowing into the peritubular capillaries in sufficient quantity when the blood flow in the glomeruli (deeper than the OCT measurement area) is blocked by microcapsules. Therefore, we registered to decrease the peritubular capillar's density in the early minutes after injection (Fig. 3(B)). However, in the case of a properly selected dosage, the blood supply to the glomeruli can be restored over time which we demonstrate in our experiment. This is most likely due

to the gradual washing out of the capsules from the glomeruli within the bloodstream, taking into account their ability to some deformation [25]. Thanks to this process, the glomeruli are completely cleared of capsules by 24 hours (Fig. 4(A)). In the case of a critically high dosage, the blood flow in the glomeruli is irreversibly blocked, and therefore the capsules are not washed out and remain in the glomeruli even after a day. Such a long-term blockade of blood flow leads to acute ischemic and further morpho-anatomical damage to the tissues of both kidneys (Fig. 3(C)).

Our experiment shows that the critical change of the peritubular capillar's density recorded in the upper layers of the renal cortex is a reflection of complex pathological processes occurring in the deeper layers (glomerular zone). Thus, the registration of pathologically low values of peritubular capillar's density by the OCT method can be used as a basis for a more detailed diagnosis of the causes of impaired renal blood supply. Timely high-quality diagnostics is the key factor to choose the right treatment strategy for various renal diseases associated with impaired blood flow.

4. Conclusion

We proposed a ready-to-use protocol that makes deep-lying internal organs available for high-precision volumetric functional OCT imaging via angiographic signal processing. The possibility of using OCT to detect circulatory disorders in the kidney was shown. The developed fixation technique in combination with proposed surgical protocol allowed us to obtain a volumetric blood flow map completely free of motion artifacts and performed 3D reconstruction of the kidney's superficial capillary network. As an example, 3D microangiography maps and volumetric vessels density datasets after capsules injection at two dosages (safe — 10×10^6 and critical — 20×10^6) are given. The drop in blood flow in the cortical layer, from where the signal was collected, was associated with the adhesion of the administered capsules to the endothelium in the vessels of the glomerular region with a kind of artificial plaques formation. As a result, a significantly smaller volume of blood entered the cortex. In the case of a safe dose, these changes were reversible and after 24 hours the blood flow returned to basal values, since the capsules were eliminated from the organ. In the case of a critical dose, the restoration of blood flow did not occur due to the retention of capsules in the kidney vessels for more than 24 hours, which in the long term led to ischemic and fibrotic changes in the entire organ. Thus, the described OCT-based blood flow analysis technique can be used to monitor the effect of drug delivery systems on blood circulation in the target kidney undergoing therapy. Proposed protocol with a combination of ultra fast (>200 kHz scan rate) OCT could be used as a surgical assistant tool for the real-time monitoring of pathological changes associated with functional disorders of the vasculature.

Disclosures. The authors declare no conflicts of interest.

Data availability. Data underlying the results presented in this paper are not publicly available at this time but may be obtained from the authors upon reasonable request.

Supplemental document. See Supplement 1 for supporting content.

References

1. R. K. Wang, "Optical microangiography: a label-free 3-D imaging technology to visualize and quantify blood circulations within tissue beds in vivo," IEEE J. Sel. Top. Quantum Electron. **16**(3), 545–554 (2010).
2. A. Mariampillai, B. A. Standish, E. H. Moriyama, M. Khurana, N. R. Munce, M. K. K. Leung, J. Jiang, A. Cable, B. C. Wilson, I. A. Vitkin, and V. X. D. Yang, "Speckle variance detection of microvasculature using swept-source optical coherence tomography," Opt. Lett. **33**(13), 1530 (2008).
3. A. Mariampillai, M. K. K. Leung, M. Jarvi, B. A. Standish, K. Lee, B. C. Wilson, A. Vitkin, and V. X. D. Yang, "Optimized speckle variance OCT imaging of microvasculature," Opt. Lett. **35**(8), 1257 (2010).
4. C.-L. Chen and R. K. Wang, "Optical coherence tomography based angiography," Biomed. Opt. Express **8**(2), 1056–1082 (2017).

5. L. M. C. Oliveira and V. V. Tuchin, *The Optical Clearing Method: A New Tool for Clinical Practice and Biomedical Engineering* (Springer Nature, 2019).

6. Y. Liu, D. Zhu, J. Xu, Y. Wang, W. Feng, D. Chen, Y. Li, H. Liu, X. Guo, and H. Qiu, "Penetration-enhanced optical coherence tomography angiography with optical clearing agent for clinical evaluation of human skin," Photodiagn. Photodyn. Ther. **30**, 101734 (2020).

7. M. J. Gora, M. J. Suter, G. J. Tearney, and X. Li, "Endoscopic optical coherence tomography: technologies and clinical applications," Biomed. Opt. Express **8**(5), 2405–2444 (2017).

8. A. Swaan, C. K. Mannaerts, B. G. Muller, R. A. A. van Kollenburg, M. Lucas, C. D. Savci-Heijink, T. G. van Leeuwen, T. M. de Reijke, and D. M. de Bruin, "The first in vivo needle-based optical coherence tomography in human prostate: a safety and feasibility study," Lasers Surg. Med. **51**(5), 390–398 (2019).

9. A. Levin, M. Tonelli, J. Bonventre, J. Coresh, J.-A. Donner, A. B. Fogo, C. S. Fox, R. T. Gansevoort, H. J. L. Heerspink, and M. Jardine, "Global kidney health 2017 and beyond: a roadmap for closing gaps in care, research, and policy," Lancet **390**(10105), 1888–1917 (2017).

10. D. A. Simonetto, P. Gines, and P. S. Kamath, "Hepatorenal syndrome: pathophysiology, diagnosis, and management," bmj **370** (2020).

11. K. Damman and J. M. Testani, "The kidney in heart failure: an update," Eur. Heart J. **36**(23), 1437–1444 (2015).

12. C. Kopitko, L. Medve, and T. Gondos, and Others, "Pathophysiology of renal blood supply," New Medicine (2016).

13. M. L. Onozato, P. M. Andrews, Q. Li, J. Jiang, A. Cable, and Y. Chen, "Optical coherence tomography of human kidney," The J. urology **183**(5), 2090–2094 (2010).

14. P. M. Andrews, Y. Chen, M. L. Onozato, S.-W. Huang, D. C. Adler, R. A. Huber, J. Jiang, S. E. Barry, A. E. Cable, and J. G. Fujimoto, "High-resolution optical coherence tomography imaging of the living kidney," Lab. Invest. **88**(4), 441–449 (2008).

15. Y. Fang, W. Gong, J. Li, W. Li, J. Tan, S. Xie, and Z. Huang, "Toward image quality assessment in optical coherence tomography (OCT) of rat kidney," Photodiagn. Photodyn. Ther. **32**, 101983 (2020).

16. J. Wierwille, P. M. Andrews, M. L. Onozato, J. Jiang, A. Cable, and Y. Chen, "In vivo, label-free, three-dimensional quantitative imaging of kidney microcirculation using Doppler optical coherence tomography," Lab. Invest. **91**(11), 1596–1604 (2011).

17. O. A. Sindeeva, R. A. Verkhovskii, A. S. Abdurashitov, D. V. Voronin, O. I. Gusliakova, A. A. Kozlova, O. A. Mayorova, A. V. Ermakov, E. V. Lengert, and N. A. Navolokin, "Effect of systemic polyelectrolyte microcapsule administration on the blood flow dynamics of vital organs," ACS Biomater. Sci. Eng. **6**(1), 389–397 (2020).

18. A. V. Ermakov, R. A. Verkhovskii, I. V. Babushkina, D. B. Trushina, O. A. Inozemtseva, E. A. Lukyanets, V. J. Ulyanov, D. A. Gorin, S. Belyakov, and M. N. Antipina, "In vitro bioeffects of polyelectrolyte multilayer microcapsules post-loaded with water-soluble cationic photosensitizer," Pharmaceutics **12**(7), 610 (2020).

19. O. Kopach, A. M. Pavlov, O. A. Sindeeva, G. B. Sukhorukov, and D. A. Rusakov, "Biodegradable microcapsules loaded with nerve growth factor enable neurite guidance and synapse formation," Pharmaceutics **13**(1), 25 (2020).

20. D. B. Trushina, R. A. Akasov, A. V. Khovankina, T. N. Borodina, T. V. Bukreeva, and E. A. Markvicheva, "Doxorubicin-loaded biodegradable capsules: temperature induced shrinking and study of cytotoxicity in vitro," J. Mol. Liq. **284**, 215–224 (2019).

21. R. A. Verkhovskii, A. A. Kozlova, O. A. Sindeeva, I. O. Kozhevnikov, E. S. Prikhozhdenko, O. A. Mayorova, O. V. Grishin, M. A. Makarkin, A. V. Ermakov, and A. S. Abdurashitov, "Lightsheet-based flow cytometer for whole blood with the ability for the magnetic retrieval of objects from the blood flow," Biomed. Opt. Express **12**(1), 380–394 (2021).

22. M. N. Zharkov, E. P. Brodovskaya, O. A. Kulikov, E. V. Gromova, V. P. Ageev, A. V. Atanova, Z. V. Kozyreva, A. M. Tishin, A. P. Pyatakov, and N. A. Pyataev, "Enhanced cytotoxicity caused by AC magnetic field for polymer microcapsules containing packed magnetic nanoparticles," Colloids and Surfaces B: Biointerfaces **199**, 111548 (2021).

23. V. Kozlovskaya, A. Alford, M. Dolmat, M. Ducharme, R. Caviedes, L. Radford, S. E. Lapi, and E. Kharlampieva, "Multilayer microcapsules with shell-chelated 89Zr for PET imaging and controlled delivery," ACS Appl. Mater. Interfaces **12**(51), 56792–56804 (2020).

24. O. Kopach, K. Zheng, L. Dong, A. Sapelkin, N. Voitenko, G. B. Sukhorukov, and D. A. Rusakov, "Nano-engineered microcapsules boost the treatment of persistent pain," Drug delivery **25**(1), 435–447 (2018).

25. A. Fery and R. Weinkamer, "Mechanical properties of micro-and nanocapsules: single-capsule measurements," Polymer **48**(25), 7221–7235 (2007).

26. D. V. Voronin, O. A. Sindeeva, M. A. Kurochkin, O. Mayorova, I. V. Fedosov, O. Semyachkina-Glushkovskaya, D. A. Gorin, V. V. Tuchin, and G. B. Sukhorukov, "In vitro and in vivo visualization and trapping of fluorescent magnetic microcapsules in a bloodstream," ACS Appl. Mater. Interfaces **9**(8), 6885–6893 (2017).

27. O. A. Mayorova, O. A. Sindeeva, M. V. Lomova, O. I. Gusliakova, Y. V. Tarakanchikova, E. V. Tyutyaev, S. I. Pinyaev, O. A. Kulikov, S. V. German, and N. A. Pyataev, "Endovascular addressing improves the effectiveness of magnetic targeting of drug carrier. Comparison with the conventional administration method," Nanomedicine: Nanotechnology, Biol. Medicine **28**, 102184 (2020).

28. E. S. Prikhozhdenko, O. I. Gusliakova, O. A. Kulikov, O. A. Mayorova, N. A. Shushunova, A. S. Abdurashitov, D. N. Bratashov, N. A. Pyataev, V. V. Tuchin, and D. A. Gorin, "Target delivery of drug carriers in mice kidney glomeruli via renal artery. Balance between efficiency and safety," J. Controlled Release **329**, 175–190 (2021).

29. F. Ronco, G. Tarantini, and P. A. McCullough, "Contrast induced acute kidney injury in interventional cardiology: an update and key guidance for clinicians," Rev. cardiovascular medicine **21**(1), 9–23 (2020).

30. T. Lenz, "Behandlung der Nierenarterienstenose im Jahr 2021," Der Internist pp. 1–9 (2021).

31. C. Lote, "Essential anatomy of the kidney," in *Principles of Renal Physiology*, (Springer, 2000), pp. 20–33.

32. K. M. Poole, D. R. McCormack, C. A. Patil, C. L. Duvall, and M. C. Skala, "Quantifying the vascular response to ischemia with speckle variance optical coherence tomography," Biomed. Opt. Express **5**(12), 4118 (2014).

33. L. A. Matveev, V. Y. Zaitsev, G. V. Gelikonov, A. L. Matveyev, A. A. Moiseev, S. Y. Ksenofontov, V. M. Gelikonov, M. A. Sirotkina, N. D. Gladkova, V. Demidov, and A. Vitkin, "Hybrid M-mode-like OCT imaging of three-dimensional microvasculature in vivo using reference-free processing of complex valued B-scans," Opt. Lett. **40**(7), 1472 (2015).

34. A. Moiseev, S. Ksenofontov, M. Sirotkina, E. Kiseleva, M. Gorozhantseva, N. Shakhova, L. Matveev, V. Zaitsev, A. Matveyev, E. Zagaynova, V. Gelikonov, N. Gladkova, A. Vitkin, and G. Gelikonov, "Optical coherence tomography-based angiography device with real-time angiography B-scans visualization and hand-held probe for everyday clinical use," J. Biophotonics **11**(10), e201700292 (2018).

35. Y. Shirasaki, T. Tsushima, T. Saika, Y. Nasu, and H. Kumon, "Kidney function after nephrectomy for renal cell carcinoma," Urology **64**(1), 43–47 (2004).

36. B. S. Kasinath, D. Feliers, K. Sataranatarajan, G. Ghosh Choudhury, M. J. Lee, and M. M. Mariappan, "Regulation of mRNA translation in renal physiology and disease," Am. J. Physiol. Physiol. **297**(5), F1153–F1165 (2009).

37. R. M. Donckerwolcke and M. J. Coppes, "Adaptation of renal function after unilateral nephrectomy in children with renal tumors," Pediatr. Nephrol. **16**(7), 568–574 (2001).